Nano Research

Open Access

Research Article

In situ observation Zn volatilization and microstructural resolution in ZIF-8-derived porous carbon for supercapacitors

Hongna Xing[1,§], Yibo Liu[1,§], Xia Deng[2], Xiao Chi[3], Yan Zong[1], Juan Feng[1], Xiuhong Zhu[1], Xinghua Li[1] ✉, Hongyang Zhao[4] ✉, and Xinliang Zheng[1] ✉

[1] *School of Physics, State Key Laboratory of Photoelectric Technology and Functional Materials, Northwest University, Xi'an 710127, China*
[2] *School of Materials & Energy, Electron Microscopy Centre of Lanzhou University, Lanzhou University, Lanzhou 730000, China*
[3] *Ganjiang Innovation Academy, Chinese Academy of Sciences, Ganzhou 341000, China*
[4] *School of Chemistry, Engineering Research Center of Energy Storage Materials and Devices, Ministry of Education, National Innovation Platform (Center) for Industry-Education Integration of Energy Storage Technology, Xi'an Jiaotong University, Xi'an 710127, China*
§ *Hongna Xing and Yibo Liu contributed equally to this work.*

Cite this article: *Nano Research*, **2026**, *19*, 94908497. https://doi.org/10.26599/NR.2026.94908497

ABSTRACT: Zn-based metal–organic frameworks (MOFs) are promising self-templates to fabricate metal-free porous carbon with large surface area and high porosity due to the abundant pore structure of their MOF parents and low boiling point of zinc metal during pyrolysis. However, the Zn volatilization process and microstructural resolution are still not clearly defined. Herein, we studied the pore structure formation mechanism of zeolitic imidazolate framework-8 (ZIF-8) derived carbon. The detailed temperature-dependent Zn volatilization process, Zn–N coordination configuration, and microstructural resolution processes were dynamically studied by *in situ* heating transmission electron microscope (TEM) and synchrotron radiation techniques. We revealed that the volatilization of Zn and N elements during pyrolysis process leads to porous carbon with large specific surface area and high microporosity. However, trace amounts of residual Zn still exist above the boiling point of Zn (907 °C), even at 1100 °C, which refreshes the viewpoint from previous literature. The residual zinc species were characterized by Cs-corrected high-angle annular dark-field scanning TEM (HAADF-STEM) image and synchrotron radiation. The results showed that the residual Zn element is uniformly anchored in the carbon skeleton as single Zn atom with Zn–N_1 configuration. Further experiments and density functional theory (DFT) calculations revealed that Zn–N_1 configuration has higher electrochemical activity than structurally symmetrical Zn–N_4. Besides, a symmetric supercapacitor was assembled using the porous carbon, which shows relatively high energy density and power density with excellent cycling stability. Electrochemical studies indicate that the specific capacitance is mainly determined by the specific surface area. This work is of great significance to deeply understand the microstructural resolution and properties of Zn-MOFs derived porous carbon, guiding their practical applications.

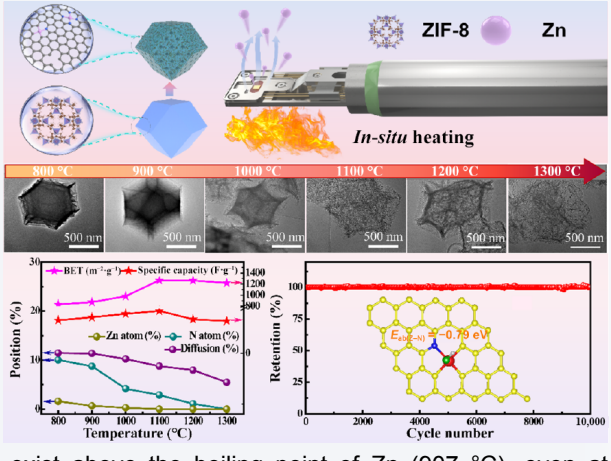

KEYWORDS: *in situ* transmission electron microscope (TEM), zeolitic imidazolate framework-8 (ZIF-8) derived carbon, single Zn atom, Zn–N configuration, synchrotron radiation, supercapacitor

1 Introduction

Heteroatom-doped porous carbon (PC) derived from metal–organic frameworks (MOFs) has drawn extensive attention in diverse fields of scientific research and practical applications due to its high specific surface area (SSA) as well as tunable structures [1, 2]. Different from traditional carbon materials, MOFs-derived porous carbon architectures possess inspiring merits, such as simple

Received: October 18, 2025; **Revised:** January 7, 2026
Accepted: January 28, 2026

✉Address correspondence to Xinghua Li, xinghua.li@nwu.edu.cn; Hongyang Zhao, zhaohy_001@xjtu.edu.cn; Xinliang Zheng, zhengxl@nwu.edu.cn

preparation, tunable particle size, and components, high specific surface area with easy heteroatom doping [3–9]. These features make the MOFs-derived porous carbon show great potential in various fields, especially in heterogeneous catalysis and energy storage/conversion systems [10–12].

Metal-free porous carbon materials are highly desired in various applications. However, most of the transition-metal-based MOFs (such as Fe, Co, Ni, Mn, Cu, Al, etc.) derived carbon needs acid treatment to eliminate the metal species [13, 14]. Meanwhile, Zn-based MOFs, particularly zeolitic imidazolate framework-8(Zn) (ZIF-8(Zn)), are inspiring precursors for the fabrication of metal-free porous carbon by pyrolysis of Zn-based MOFs in inert atmosphere at 900–1100 °C owing to the low boiling point of Zn (907 °C) and low vapor pressure [15–21]. However, the core scientific issue regarding Zn volatilization behavior during Zn-MOF pyrolysis remains controversial and insufficiently explored. Early studies proposed that Zn would be completely volatilized above its boiling point (907 °C), thereby enabling direct synthesis of metal-free porous carbon [22–24]. For instance, Park et al. [21] first reported the thermal stability of ZIF-8 and inferred complete Zn removal at temperatures > 900 °C, a conclusion later supported by Gadipelli et al. [16] in ZIF-derived carbon for CO_2 capture. Nevertheless, recent investigations have implied the potential presence of Zn residues but have not yet clarified their chemical state or stabilization mechanism. Yang et al. [13] reported single Zn atoms in MOF-derived carbon, yet did not link this to Zn volatilization behavior or confirm their existence above 907 °C. While Wang et al. [15] systematically investigated the evolution of porphyrin-like ZnN_4 centers during the pyrolysis of ZIF-8. However, the information, such as elemental composition and pore evolution, was not taken into account, and the temperature range was also limited in scope (500 to 900 °C). Moreover, a critical limitation of most previous studies lies in their reliance on *ex situ* characterization techniques, which fail to capture the real-time dynamic processes of Zn migration, volatilization, and residual state during pyrolysis [13, 14, 16–19]. This lack of *in situ* investigations has resulted in several pivotal unresolved issues: (1) Whether Zn can genuinely persist in the carbon matrix above 907 °C; (2) if so, what coordination environment stabilizes Zn against volatilization. Consequently, despite extensive efforts devoted to preparing metal-free porous carbon from Zn-based MOFs, in-depth understanding of the formation mechanism of such carbon materials remains inadequate. *In situ*, real-time, and dynamic investigations into the microstructural evolution of Zn-MOFs during pyrolysis are therefore imperative to fill these knowledge gaps, which are crucial for elucidating the formation mechanism of Zn-MOF-derived carbon and maximizing its electrochemical performance.

Herein, for the first time, the structural evolution of ZIF-8-derived porous carbon architectures was dynamically studied in real-time. The volatilization of Zn and variation of porosity were investigated by *in situ* heating, TEM, and *ex situ* characterization. The state of residual Zn and N elements in carbon skeleton was characterized by synchrotron radiation and atomic resolution STEM techniques. In addition, the porous carbon architectures were used as electrode material for supercapacitors. This work offered an opportunity to understand the microstructural resolution and properties of Zn-MOFs-derived porous carbon, guiding their practical applications.

2 Experimental section

2.1 Chemicals

Zinc nitrate hexahydrate ($Zn(NO_3)_2{\cdot}6H_2O$) was bought from Shanghai Sinopharm Chemical Reagent Co., Ltd. 2-Methylimidazole ($C_4H_6N_2$) was purchased from Aladdin. Methanol was obtained from Guangdong Guanghua Sci-Tech Co., Ltd. Carbon cloth (CC) was bought from Taiwan Carbon Energy Technology Co., Ltd. All the chemicals were used without any further purification.

2.2 Synthesis of ZIF-8

4 mmol of $Zn(NO_3)_2{\cdot}6H_2O$ and 32 mmol of 2-methylimidazole were separately dissolved into 40 mL of methanol, respectively. The Zn^{2+}-containing solution was slowly added into the 2-methylimidazole-containing solution. The resulting solution was magnetically stirred for 30 min, and then allowed to stand for 24 h at room temperature. White precipitate was obtained by filtration, washed with ethanol three times, and then dried at 60 °C.

2.3 Synthesis of porous carbon architectures

Porous carbon was fabricated by pyrolysis of ZIF-8 in Ar at different temperatures, during which the heating rate and pyrolysis time were set to be 2 °C·min^{-1} and 2 h, respectively. By changing the pyrolysis temperature to 800, 900, 1000, 1100, and 1300 °C, the products were marked as PC-800, PC-900, PC-1000, PC-1100, PC-1200, and PC-1300, respectively.

2.4 *In situ* heating TEM of ZIF-8

ZIF-8 was placed on the Si_3N_4 electron-transparent chips (E-chips), and then loaded into a heating TEM holder (Fusion 350, Protochips, USA), which has a maximum reliable operating temperature of 1200 °C due to the hardware limitation. The *in situ* heating TEM experiment was carried out in aberration-corrected electron microscope (Spectra 300, Thermo Scientific, USA) at 300 kV. To avoid potential sample damage or data inaccuracy from pushing the equipment to its upper limit, the *in situ* heating temperatures were set at 800, 900, 1000, and 1100 °C with a heating rate of 10 °C·min^{-1} for characterization.

2.5 Characterizations

The phases of samples were examined by X-ray diffraction (XRD) instrument (Bruker D8 Advance, Cu Kα). The morphology was characterized by scanning electron microscope (SEM, Apreo S, ThermoFisher Scientific), transmission electron microscope (TEM, Tecnai G^2 F20, FEI), and spherical aberration-corrected electron microscope (Titan Cubed Themes G2 300, FEI). The elemental states were carried out by X-ray photoelectron spectroscopy (XPS, ESCALAB210). The disorder states of carbon were analyzed by Raman spectra (inVia Reinishaw confocal spectrometer) with a laser of 633 nm. The decomposition curve of ZIF-8 was examined by thermo-gravimetric analyzer (TGA, STA 449C, NETZSCH) in N_2. The N_2 absorption/desorption isotherms were analyzed by a JW-BK100 instrument (Beijing JWGB Sci. & Tech. Co., Ltd.).

2.6 Calculation method

The molecular dynamics (MD) simulations were performed using the Vienna *ab initio* simulation package (VASP) to calculate bond energy, total potential energy, and radial distribution function

(RDF). The temperature was maintained at 800, 1400, and 1600 K, respectively, by the Anderen thermostat method during simulations. The time step was set to 1 fs to integrate the equations of motion.

2.6.1 *Density functional theory (DFT) calculations*

All the spin-polarized first-principles calculations were also performed via VASP. The ion–electron interactions were described by the projector augmented wave (PAW) method, and the generalized gradient approximation (GGA) with the Perdew–Burke–Ernzerh (PBE) functional was employed for the exchange-correlation energy. A plane-wave cutoff energy of 450 eV was used. The self-consistent field iterations converged when the energy change was below 1×10^{-5} eV per atom.

2.7 Electrochemical characterization

The electrochemical characterization was operated in a conventional three-electrode electrochemical cell, using a CHI660E electrochemical working station (Shanghai Chenhua Science Technology Corp., Ltd.). A saturated Hg/HgO electrode and a platinum plate served as reference and counter electrodes, respectively. The working electrode was fabricated by mixing the porous carbon, polytetrafluoroethylene (PTFE) binder, and acetylene black with a weight ratio of 8:1:1, during which CC (1 cm × 2 cm). The loading mass of N-doped porous carbon (N-doped PC) was 2 mg for all the electrodes. Then all the coated electrodes were dried at 60 °C in the vacuum drying oven for 6 h. 6 M KOH was used as the electrolyte. The potential window was set from 0 to −1.0 V. The electrochemical impedance spectroscopy (EIS) measurement was performed by applying an alternating current (AC) voltage of 5 mV in a frequency range of 0.01 Hz to 1000 kHz. Furthermore, a symmetric supercapacitor (SSC) was constructed using PC-1100 as both the positive and negative electrode materials.

3 Results and discussion

ZIF-8 was fabricated by a modified stationary precipitation route at room temperature. Figure S1(a) in the Electronic Supplementary Material (ESM) illustrates the topological structure of ZIF-8. Tetrahedral ZnN_4 nodes are linked via imidazolate ligands through Zn–N coordination, forming four-membered rhombic rings that further extend and assemble into a three-dimensional topological frameworks. The structure shows large cages (11.6 Å) connected through six-membered apertures (3.4 Å) [21]. XRD pattern (Fig. S1(b) in the ESM) shows a sodalite topology of cubic structure (a = 16.97 Å and space group: $I\bar{4}3m$) with a chemical formula of $Zn(C_4H_6N_2)_2$, which matches well with the simulated data. The N_2 adsorption–desorption isotherm (Fig. S1(c) in the ESM) behaves as a reversible Type-I isotherm with an abrupt rise of N_2 uptake at a low relative pressure (P/P_0 < 0.01), suggesting the microporous characteristic. The Brunauer–Emmett–Teller (BET) specific surface area and porous volume are 1285 $m^2 \cdot g^{-1}$ and 0.66 $cm^3 \cdot g^{-1}$, respectively, which are consistent with the reported values [25, 26]. SEM image (Fig. S1(d) in the ESM) shows that the ZIF-8 crystals exhibit rhombic dodecahedral morphology with a uniform size of about 2 μm, exposing eight {110} faces and six {100} faces. To further characterize the nanostructure of ZIF-8 at atomic scale, low-dose high-resolution TEM (HRTEM) technique was adopted, and the images were collected by correcting the contrast transfer function (CTF) of objective lens, as reported by Han and co-workers [27, 28]. Figures S1(e) and S1(f) in the ESM display the crystal structure diagram and CTF-corrected HRTEM images of ZIF-8 obtained from the crystallographic orientation of <111> axis. A highly ordered stacking structure with hexagonal arrangement can be seen. The white dots are the microporous cages of ZIF-8, which are surrounded by six black metal nodes of zinc clusters. This is consistent with the crystalline structure of ZIF-8.

Porous carbon was synthesized by pyrolysis of ZIF-8 in Ar at different temperatures. Figure 1(a) shows the XRD patterns of PC materials prepared at 800–1300 °C. The two broad diffraction peaks located at about 25.1° and 43.5° suggest the amorphous characteristic of carbon. No other diffraction peaks related to Zn-related materials, such as Zn metal or ZnO, are detected. By increasing the annealing temperature, the peak intensity is stronger, and the full width at half maximum (FWHM) is narrower. This indicates that improving the pyrolysis temperature can enhance the graphitization degree of ZIF-8-derived PC materials. Furthermore, the graphitization degree of PC materials was examined by Raman spectra (Fig. S2 in the ESM). The two peaks at 1355 and 1585 cm^{-1} correspond to the disordered D and ordered G bands of carbon, respectively [29, 30]. The D band is attributed to the in-plane vibration of sp^2 hybridized carbon, and its intensity is related to the structural defects and doped N. The G band is assigned to the in-plane stretching vibration of sp^2 hybridized carbon, attributed to the ordered structure of carbon. The relative intensity ratio of D and G bands (I_D/I_G) is decreased as the pyrolysis temperature increases, suggesting that the defects are reduced and the degrees of graphitization are enhanced.

SEM images (Fig. S3 in the ESM) reveal that the ZIF-8-derived PC materials change from rhombic dodecahedron to near-spherical shape by increasing the pyrolysis temperature, during which the carbon framework collapses with increased wrinkles on the surface. The chemical compositions and elemental states were further characterized by energy-dispersive X-ray spectrometry (EDX) and XPS techniques. The EDX spectra (Fig. S4 in the ESM) show several characteristic X-ray peaks at 0.28, 0.39, 0.52, 1.01, and 1.74 eV, corresponding to the C Kα, N Kα, O Kα, Zn Lα, and Si Kα, respectively. The O signal is mainly due to the absorbed oxygen or surface oxidation. The Si signal is attributed to the Si substrate for measurement. Figure S5 in the ESM shows the full scan XPS spectra of ZIF-8-derived PC materials. The peaks with binding energies of about 285, 400, 530, and 1024 eV are assigned to C 1s, N 1s, O 1s, and Zn 2p, respectively. The element contents obtained by EDX and XPS spectra are summarized in Table S1 in the ESM. Figure 1(b) shows the high-resolution N 1s and Zn 2p XPS spectra. Based on the results, four conclusions can be found: (1) The N and Zn signals decrease by increasing the pyrolysis temperature; (2) N element disappears at 1300 °C; (3) Zn signal completely disappears at 1200 °C; (4) Zn element is still residual in the PC materials even at 1100 °C. These results are different from the reported works: It is generally accepted that pyrolysis of Zn-MOFs can directly result in the fabrication of metal-free porous carbon, only when the temperature is higher than 907 °C (the boiling temperature of Zn) [21, 24]. The discrepancy mainly arises from two factors: First, previous studies adopted *ex situ* XRD characterization with limited sensitivity to trace single-atom Zn; second, they ignored the potential stabilization effect of N coordination on Zn, which we confirm as Zn–N configuration. In addition, the atomic ratios of Zn/C and N/C obtained by XPS technique are smaller than those from EDX technique. This suggests that the Zn and N elements at

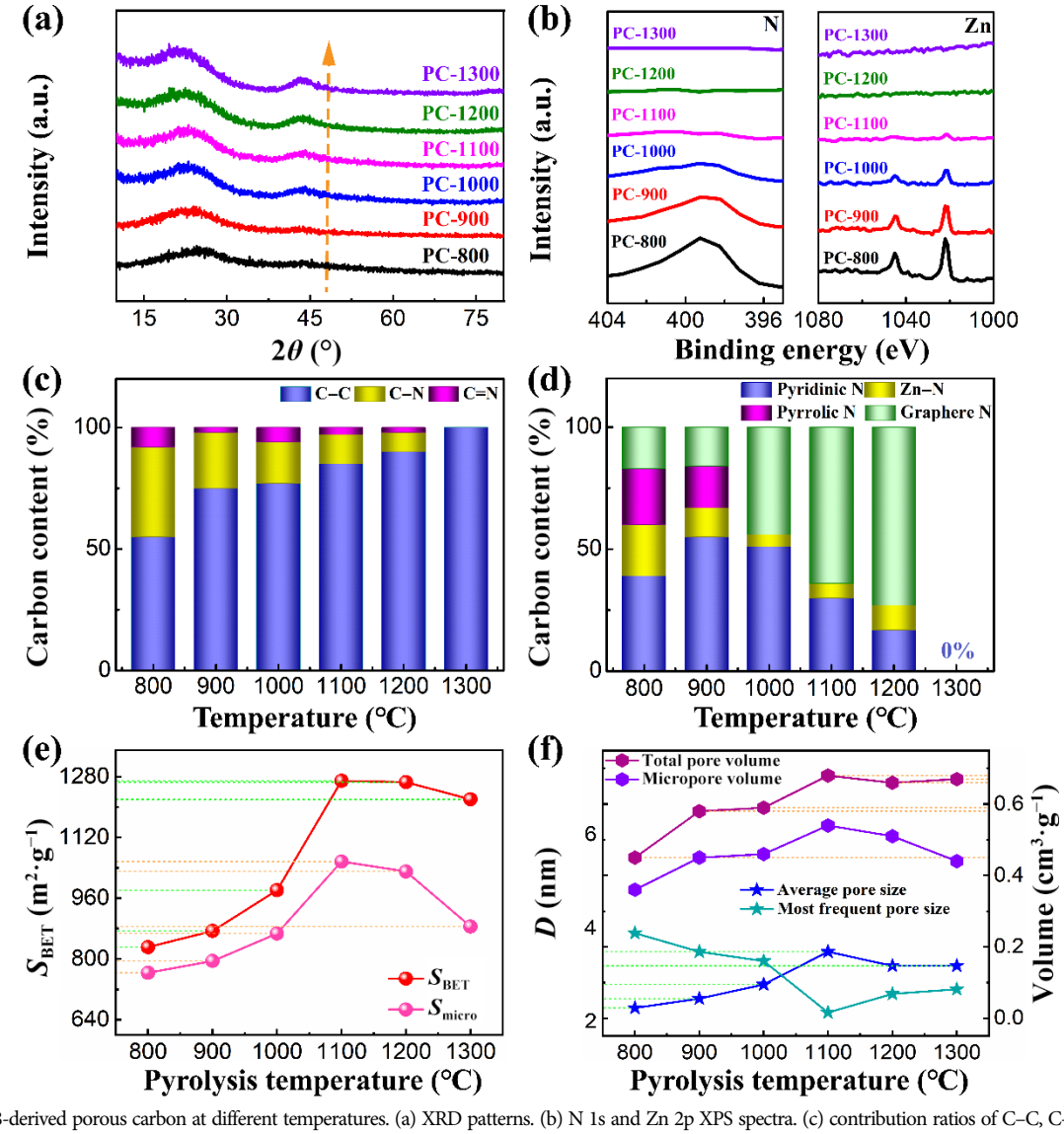

Figure 1 ZIF-8-derived porous carbon at different temperatures. (a) XRD patterns. (b) N 1s and Zn 2p XPS spectra. (c) contribution ratios of C–C, C–N, and C=N by fitting C 1s spectra. (d) Contribution ratios of pyridinic N, Zn–N, pyrrolic N, and graphitic N by fitting N 1s spectra. (e) S_{BET} and S_{micro}. (f) Pore volumes, micropore volumes, average pore size, and most frequent pore size obtained by N_2 sorption/adsorption isotherms and pore-size distribution curves.

the surface of carbon skeleton are more easily volatilized by pyrolysis treatment. To verify the elemental states in ZIF-8-derived PC materials, high-resolution XPS spectra are analyzed in Fig. S6 in the ESM. Table S2 in the ESM summarizes the ratios of functional groups. The C 1s spectra (Figs. S6(a1)–S6(a6) in the ESM) can be fitted by three characteristic peaks: C–C graphite carbon at 284.8 eV, C–N group at 285.6 eV, and C=N group at 286.8 eV [31, 32]. Figure 1(c) illustrates the histogram of carbon-based groups in ZIF-8-derived PC materials. By increasing the pyrolysis temperature, the contents of C–C group increase, and the C–N/C=N groups are reduced. When the pyrolysis temperature reaches up to 1300 °C, only C–C group is observed in PC-1300. Figs. S6(b1)–S6(b6) in the ESM show the N 1s spectra of ZIF-8-derived PC materials. The signal-to-noise ratio decreases by increasing the pyrolysis temperature, indicating that N content is decreased in the PC materials. The N element has disappeared in PC-1300. The N 1s spectra can be assigned to four species at 398.2, 399.6, 400.2, and 401.1 eV, related to pyridine N, Zn–N, pyrrole N, and graphite nitrogen, respectively. Zn element is present as Zn–N bond in the ZIF-8-derived PC materials. The corresponding histogram of nitrogen-based groups is displayed in Fig. 1(d). By improving the pyrolysis temperature, the ratio of graphite nitrogen increases, while the amounts of pyridine N and pyrrole N decrease. Zn–N bond disappears at 1200 °C. The Zn 2p spectra are shown in Figs. S6(c1)–S6(c6) in the ESM. As the pyrolysis temperature increases, the signal-to-noise ratio of Zn 2p decreases, suggesting that Zn content is decreased. The Zn element is totally volatilized when the temperature is higher than 1200 °C. Due to the different energies of excited electrons, the detection depths of XPS and EDX techniques are 1–2 μm and 1–10 nm, respectively.

To characterize the specific surface area and porosity, the N_2 adsorption/desorption isotherms are shown in Fig. S7(a) in the ESM. All the curves show Type-IV isotherm with H3-type hysteresis loop. The distinct N_2 uptake at extremely low pressure ($P/P_0 \leq 0.01$) suggests the presence of plentiful micropores. The obvious hysteresis phenomenon at moderate pressure ($0.4 \leq P/P_0 \leq 0.9$) indicates the existence of mesopores. The specific surface areas were calculated by BET method. The pore-size distributions were

obtained according to Barrett–Joyner–Halenda (BJH) method, as shown in Fig. S7(b) in the ESM. Table S3 in the ESM summarizes the textural parameters of ZIF-8-derived PC materials, including specific surface areas, pore volumes (V_{total}), and pore sizes. The BET specific surface areas (S_{BET}) and average pore sizes (D_{AV}) climb up and then decline as the pyrolysis temperatures increase. We consider that this phenomenon is caused by the combined effects of Zn volatilization and skeleton collapse, which have been demonstrated by the SEM and EDX data. The line chart graphically compared the total S_{BET}, micropore surface areas (S_{micro}), V_{total}, micropore volume (V_{micro}), D_{AV}, and the most frequent pore diameter (D_{MFPD}) of ZIF-8-derived PC materials (Figs. 1(e) and 1(f)). The specific surface area is a function of both pore size and number/volume, and the surge in micropore number/volume dominates the specific surface area enhancement. The specific surface area and pore volume present the "increase-then-decrease" trend as the pyrolysis temperature increases. The ZIF-8-derived PC material prepared at 1100 °C (PC-1100) shows the highest S_{BET} value of 1269.1 $m^2 \cdot g^{-1}$ and V_{total} value of 0.68 $cm^3 \cdot g^{-1}$. This temperature-dependent variation originates from the synergistic but competing effects of two processes: (1) Zn volatilization, which creates new pores and expands existing pores (pore-forming); (2) thermal-induced carbon framework collapse or rearrangement, which reduces pore volume and merges small pores (pore-destroying). For 800–1100 °C, Zn volatilization dominates and generates abundant micropores by creating voids (Table S3 in the ESM: Micropore volume increases from 0.36 for PC-800 to 0.54 $cm^3 \cdot g^{-1}$ for PC-1100), leading to a sharp specific surface area rise (830.9 to 1269.1 $m^2 \cdot g^{-1}$). This confirms that SSA enhancement is dominated by increased pore number rather than pore size expansion. These results are also confirmed by the SEM (Fig. S3 in the ESM) and following *in situ* TEM (Fig. 2(b)) results. The carbon framework retains partial dodecahedral morphology with increasing translucency (due to Zn loss), but no significant collapse is observed, confirming that pore-forming from Zn volatilization outweighs minor framework rearrangement. At 1100–1200 °C, Zn volatilization nears completion (XPS, Fig. 1(b)), and the pore-forming effect weakens to a dynamic equilibrium with minor framework rearrangement, resulting in the maximum specific surface area of PC-1100. Above 1200 °C, complete Zn volatilization eliminates pore formation, while high pyrolysis temperature induces severe framework collapse (SEM in Fig. S3 in the ESM, following TEM in Fig. S8 in the ESM). This causes micropore coalescence and pore volume reduction (Table S3 in the ESM: Total pore volume drops from 0.68 for PC-1100 to 0.57 $cm^3 \cdot g^{-1}$ for PC-1300), leading to decreased specific surface area and slightly reduced most frequent pore diameter. These results demonstrate that the specific surface area and pore structure of ZIF-8-derived carbon are governed by the temperature-dependent balance between Zn volatilization and framework evolution. High specific surface area is fascinating for electronic double-layer capacitor (EDLC). Generally, the electrochemical performance of EDLC is determined by the specific surface area and porosity [33–35]. Large specific surface area can supply abundant active sites to physically absorb electrolyte ions. The porosity can serve as channels and vessels for the diffusion and storage of ions. The micropores are advantageous for the diffusion and absorption of ions, resulting in large capacitance. The mesopores are beneficial to shorten the ion transport path, leading to high capacity [36, 37].

TEM technique has high spatial and compositional resolution, which is adopted to analyze the microstructure evolution of materials at nanoscale. Figure 2(a) shows a schematic illustration of the *in situ* TEM heating experiment. The setup consists of a heating holder equipped with a microfabricated heating chip. The ZIF-8 was heated *in situ* from 200 to 1100 °C, and its nanostructure changed with the volatilization of Zn atoms. The TEM images of ZIF-8-derived PC materials prepared at different temperatures are shown in Fig. 2(b). The real-time *in situ* TEM video of ZIF-8 pyrolysis from 200 to 1100 °C can be seen from Video S1 in the ESM. With the increase of pyrolysis temperature, the rhombic dodecahedron structure collapses and shrinks, especially at the edge of framework. Besides, the skeleton gradually becomes translucent. This is mainly attributed to the volatilization of Zn element. The XRD patterns and TEM images clearly indicate that no obvious Zn-based particles or clusters are found in the skeleton of ZIF-8-derived PC materials. To further dynamically characterize the structural evolution and element distribution of ZIF-8-derived PC materials, *in situ* heating TEM technique is used. The real-time dynamic pyrolysis process of ZIF-8 is recorded by *in situ* heating TEM, as shown in Video S1 in the ESM. Since the *in situ* heating holder can be heated up to 1200 °C, the data was collected in the temperature range of 200–1100 °C. As displayed in the high-angle annular dark-field scanning TEM (HAADF-STEM) images, the particle size becomes smaller. This indicates that the framework collapses by increasing the heating temperature. The EDX elemental mappings show that the C, N, and Zn elements are uniformly distributed in the whole framework.

The N and Zn signals gradually weaken as the heating temperature increases (Fig. 2(c)), indicating progressive volatilization of these elements. Notably, Zn is still detectable at 1100 °C, which is inconsistent with *ex situ* observations, which reported no Zn residues above 1000 °C [15, 18]. This difference stems from the real-time tracking capability of *in situ* heating TEM: *Ex situ* techniques can only capture the final state of the product, while *in situ* observation reveals the dynamic residual behavior of Zn, which is stabilized by the formation of Zn–N bonds (as confirmed by XPS and synchrotron radiation results below). To further characterize the compositional resolution, the HAADF-STEM images and EDX elemental mappings of PC-1200 and PC-1300 are examined, as displayed in Fig. S8 in the ESM (*ex situ* TEM experiments results). Zn signal has disappeared in PC-1200, and N signal is absent in PC-1300. These results are consistent with the above characterizations and match well with the XPS results. Combined with the above SEM, XPS, and BET results (Fig. S3 in the ESM and Fig. 1), we suppose that the morphological evolution of ZIF-8-derived porous carbon (framework collapse) is tightly coupled with the role of Zn–N bonds in framework stability.

Owing to the high sensitivity to electronic and geometric structure, synchrotron radiation technique was used to identify the coordination environment and valence state of Zn element. Figure 3(a) shows the Zn K-edge X-ray absorption near-edge structure (XANES) spectra of ZIF-8-derived PC materials, during which ZnO and Zn foil were used as the references. The absorption threshold of ZIF-8-derived PC materials is located between metallic Zn foil and ZnO, indicating that the valence states of Zn ions are between 0 and +2. After wavelet transform, the Fourier transforms of k^2-weighted Zn K-edge extended X-ray absorption fine structure (EXAFS) spectra are displayed in Fig. 3(b). All the samples show a similar peak at about 1.50 Å, suggesting the Zn–N_x coordination. No fingerprint signal peaks of Zn–Zn interaction in Zn foil (2.30 Å)

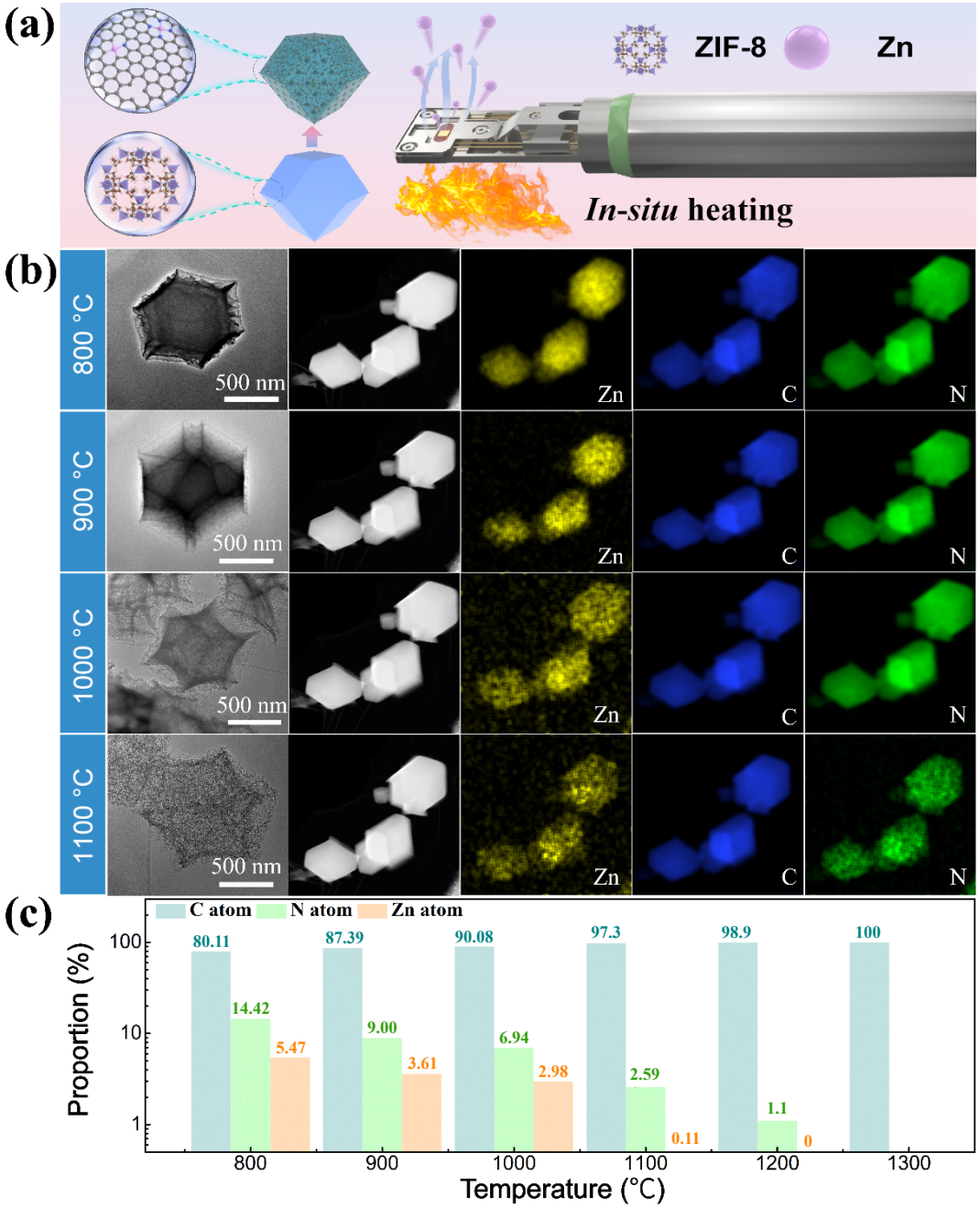

Figure 2 (a) Schematic illustration of *in situ* heating TEM experimental setup. (b) TEM images of ZIF-8-derived PC materials, corresponding HAADF-STEM images, and EDX elemental mapping images, which were recorded during the *in situ* heating treatment of ZIF-8 in TEM at 800–1100 °C. (c) Histograms of the element contents of C, N, and Zn elements given by EDX.

and ZnO (2.90 Å) were observed, suggesting that Zn was atomically distributed in the ZIF-8-derived PC materials. The fitting EXAFS curves of PC-1100 in *k* and *R* spaces (Figs. 3(c) and 3(d)) suggest that Zn–N configuration is the dominating coordination structure in ZIF-8-derived PC materials. Based on the EXAFS fittings (Fig. S9 in the ESM), the corresponding parameters of ZnNC structure were provided as shown in Table S4 in the ESM. Parameters display the coordination number (*N*) of PC-800 and PC-1100 are 0.91 and 1.04, respectively, both close to 1.0. This is preliminary confirmation that the coordination structure is Zn–N_1 model in ZnNC. Atomic resolution HAADF-STEM image of PC-1100 (Fig. 3(e)) clearly indicates that single Zn atoms are evenly dispersed in the carbon skeleton. Figure 3(f) shows the schematic model of Zn environment from the top and side views. Zn element in the ZIF-8-derived PC materials is present as single atom with Zn–N_1 coordination. In addition, it is well known that Zn can be volatilized when the temperature exceeds its boiling point (907 °C). However, Zn element can still be detected even if the pyrolysis temperature reaches 1100 °C. These results suggest that N atoms in the carbon skeleton form stable Zn–N_1 bonds, which not only inhibit the aggregation of Zn into particles but also enhance the high-temperature stability of Zn, even above its boiling point (907 °C).

To deepen the theoretical understanding of the enhanced

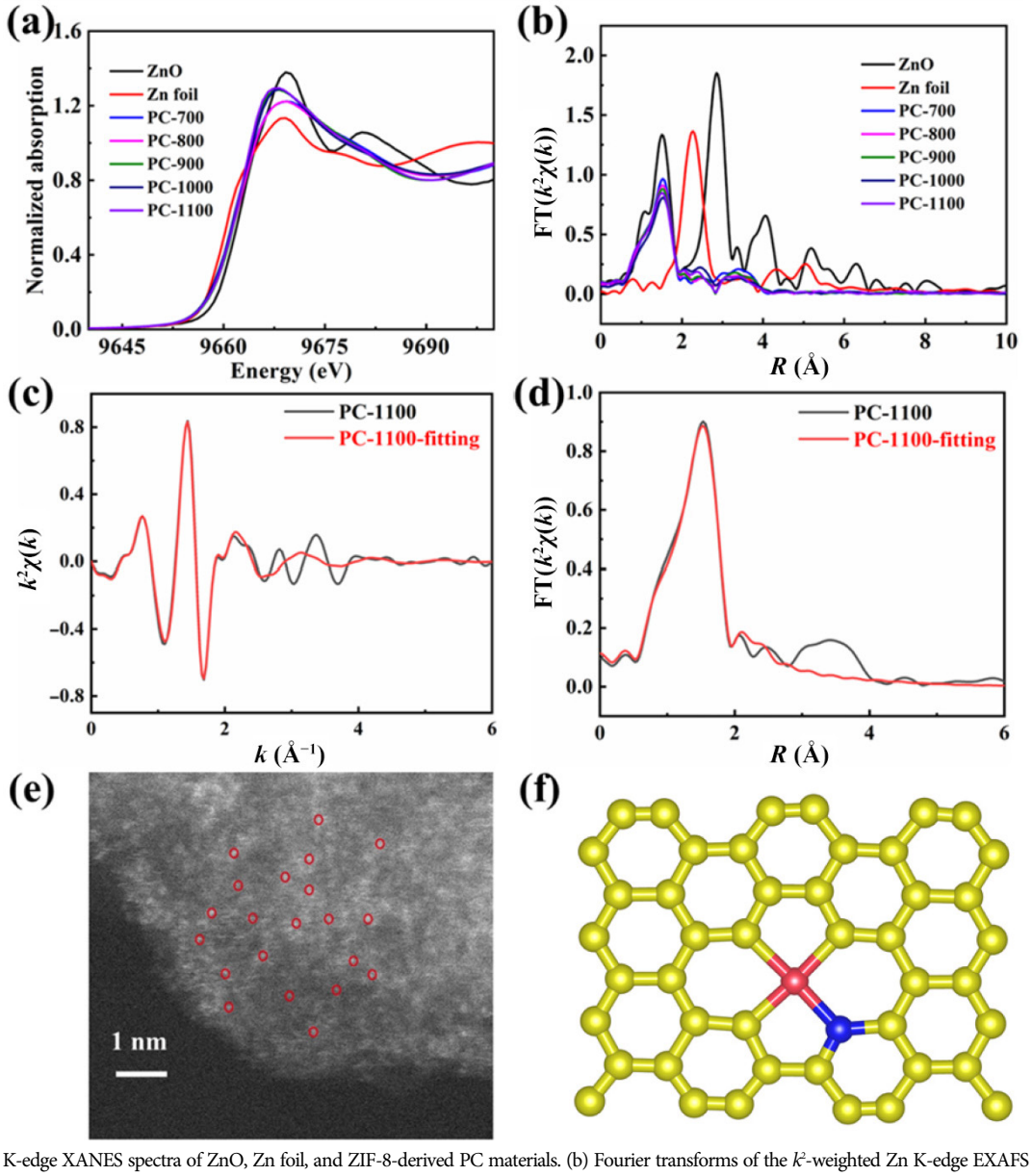

Figure 3 (a) Zn K-edge XANES spectra of ZnO, Zn foil, and ZIF-8-derived PC materials. (b) Fourier transforms of the k^2-weighted Zn K-edge EXAFS spectra. ((c) and (d)) Fitting EXAFS curves of PC-1100 in k and R spaces. (e) Atomic resolution HAADF-STEM image of PC-1100. (f) Schematic model of Zn environment from the top and side views.

stability of Zn and the temperature-dependent evolution of Zn–N coordination (consistent with our experimental observations), MD simulations were supplemented. Given that a single ZIF-8 unit cell contains 348 atoms, full-unit-cell calculations using VASP are computationally prohibitive. Leveraging the high structural symmetry of ZIF-8, we selected a representative 72-atom structural motif (2Zn, 14N, 28C, and 28H) to simulate atomic-scale dynamics under temperatures matching our experimental pyrolysis conditions (800 K = 500 °C, 1400 K = 1100 °C, and 1600 K = 1300 °C). The MD results (Fig. 4) provide direct theoretical insights into the temperature-dependent stability of Zn–N bonds, with excellent consistency with experimental data. Notably, the Zn–N bond energy in ZIF-8 (−1.28 kcal·mol^{-1}) is ~ 4.6 times more negative than the Zn–Zn cohesive energy in metallic Zn (−0.28 kcal·mol^{-1}). This confirms that Zn–N coordination in the ZIF-8 framework is thermodynamically more favorable and resistant to thermal cleavage than metallic Zn, laying the intrinsic energetic foundation for the stability of Zn above its boiling point (Fig. 4(a)). Furthermore, the potential energy evolution of the system (Fig. 4(b)) reveals distinct kinetic behaviors at different temperatures: At 800 K (= 500 °C), the potential energy remains stable with minimal fluctuations, indicating that thermal energy is insufficient to overcome the activation barrier for Zn–N bond cleavage; at 1400 K (= 1100 °C), abrupt energy drops are observed, corresponding to decomposition of the ZIF-8 framework and partial cleavage of Zn–N bonds, during which residual Zn atoms retain stable Zn–N coordination (consistent with EXAFS results confirming Zn–N_1 configuration); at 1600 K (= 1300 °C), intense energy fluctuations and continuous bond cleavage lead to complete Zn volatilization, in line with XPS data showing no Zn signal in PC-1300. Finally, the Zn–N RDF further validates structural evolution (Fig. 4(c)): Sharp RDF peaks at 800 K reflect the retained ordered

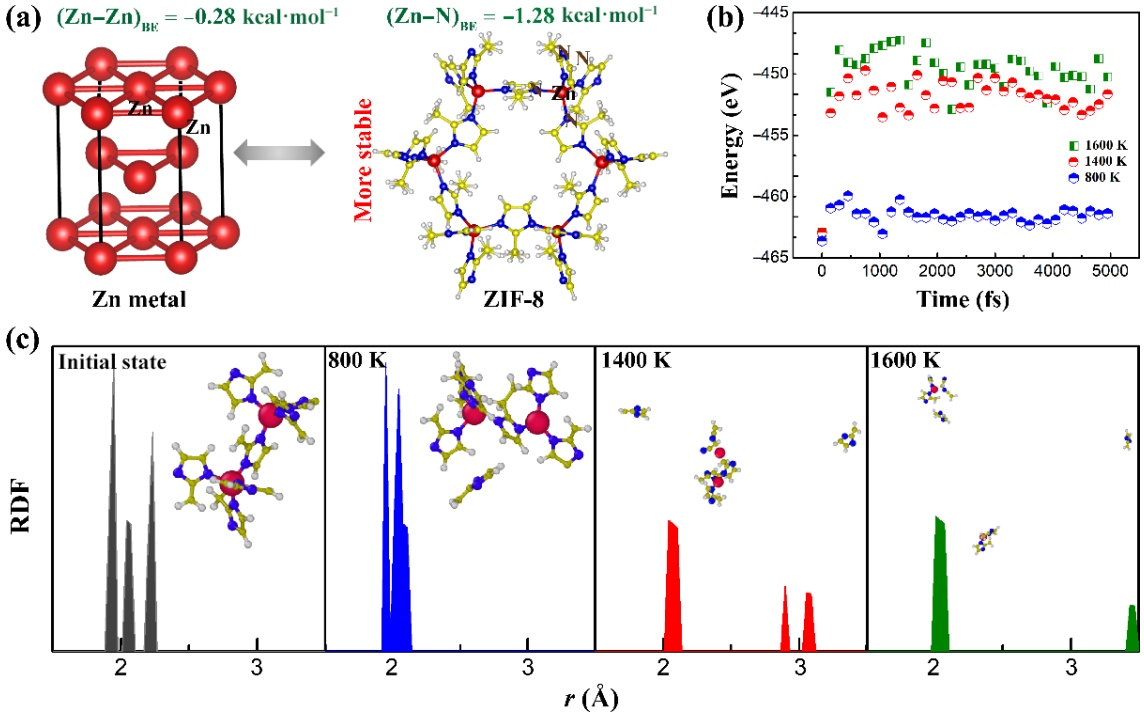

Figure 4 Molecular dynamics simulation: (a) Comparison of Zn–Zn bond energy in elemental zinc and Zn–N bond energy in ZIF-8. (b) The total potential energy of the system at three different temperatures (800, 1400, and 1600 K). (c) Zn–N radius distribution function (RDF) at initial state (0 K), 800, 1400, and 1600 K. Inset is the evolution of the crystal structure of system under the corresponding temperature conditions.

framework; broadening and rightward shifting of the first peak at 1400 and 1600 K indicate altered coordination environments and reduced Zn–N coordination number (Zn–N bonds were broken). The corresponding video of the structural evolution is available in Videos S2–S4 in the ESM. Collectively, these MD simulation results are fully consistent with our experimental observations (e.g., EXAFS-derived Zn–N_1 configuration, XPS-detected Zn residual at 1100 °C, TEM-observed framework evolution). Based on the integrated experimental and MD simulation analysis, the enhanced stability of Zn above 907 °C originates from two mutually reinforcing factors: (1) the inherently high Zn–N bond energy, which confers thermodynamic stability superior to metallic Zn; (2) the spatial confinement effect of the carbon skeleton, which inhibits Zn atom diffusion/aggregation and promotes the formation of stable low-coordination Zn–N configurations.

Owing to the large specific surface area, porous structure and rich N dopant, ZIF-8-derived porous carbon materials are promising electrode materials for double-layer electrochemical capacitors (DELCs). The electrochemical performance was measured by a three-electrode system. Figure 5(a) shows the galvanostatic charge–discharge (GCD) curves of the ZIF-8-derived PC materials at a current density of 1 A·g^{-1}. All the samples show a triangular shape with good symmetry, suggesting the typical EDLC characteristic. Based on the GCD curves, the specific capacitance (C (F·g^{-1})) can be calculated by Eq. (1) [38, 39]

$$C = \frac{It}{\Delta V m} \quad (1)$$

where I (A), t (s), ΔV (V), and m (g) are the discharging current, discharging time, potential window, and mass of ZIF-8-derived PC materials in the electrode, respectively. The specific capacitances at 1 A·g^{-1} are 163, 178, 195, 210, 168, and 160 F·g^{-1} for PC-800, PC-900, PC-1000, PC-1100, PC-1200, and PC-1300, respectively. The specific capacitance values of ZIF-8-derived PC materials increase first and then decrease as the pyrolysis temperature increases. PC-1100 shows the highest specific capacitance value with the longest discharge time. The cyclic voltammetry (CV) curves of ZIF-8-derived PC materials (Fig. S10(a) in the ESM) show a nearly rectangular shape, further indicating the EDLC feature. PC-1100 shows the largest integral area of CV curve, indicating the highest specific capacitance among the ZIF-8-derived PC materials. Figure S10(b) in the ESM shows the enlarged area circled by the cyan line (–0.15–0 V) of the CV curves. In which the capacity increases gradually with the increase in curve polarization. Among them, the curve polarization of PC-1100 is most obvious. Figure 5(b) displays the Nyquist impedance plots of ZIF-8-derived PC materials. The equivalent circuit diagram (inset of Fig. 5(b)) is fitted by the ZView software. R_s, R_{ct}, W_0, and C_{dl} are the equivalent series resistance, charge transfer resistance, Warburg impedance, and double-layer capacitance, respectively [36]. R_s (the intercept with the X-axis) consists of the resistance of electrolyte, intrinsic resistance of electrode and their contact resistance. R_{ct} (diameter of the semicircular part) suggests the charge transfer process at the interface of electrode and electrolyte. W_0 (linear portion at the low frequency) indicates the charge diffusion process of electrolyte ions in electrode material. Table S5 in the ESM summarizes the R_s, R_{ct}, and W_0 values of ZIF-8-derived PC materials. PC-1100 shows the smallest R_s and R_{ct} values. The presence of C–N functional group can enhance the wettability of ZIF-8-derived PC materials in electrolyte, reducing the contact resistance. Graphitization can improve the conductivity of carbon materials. As we proved before, increasing the pyrolysis temperature can reduce the content of C–N functional group and increase the graphitization degree of ZIF-8-derived PC materials. Their competitive effect makes PC-1100 process the smallest R_s value. The large specific surface area and high porous structure can provide abundant active sites to adsorb

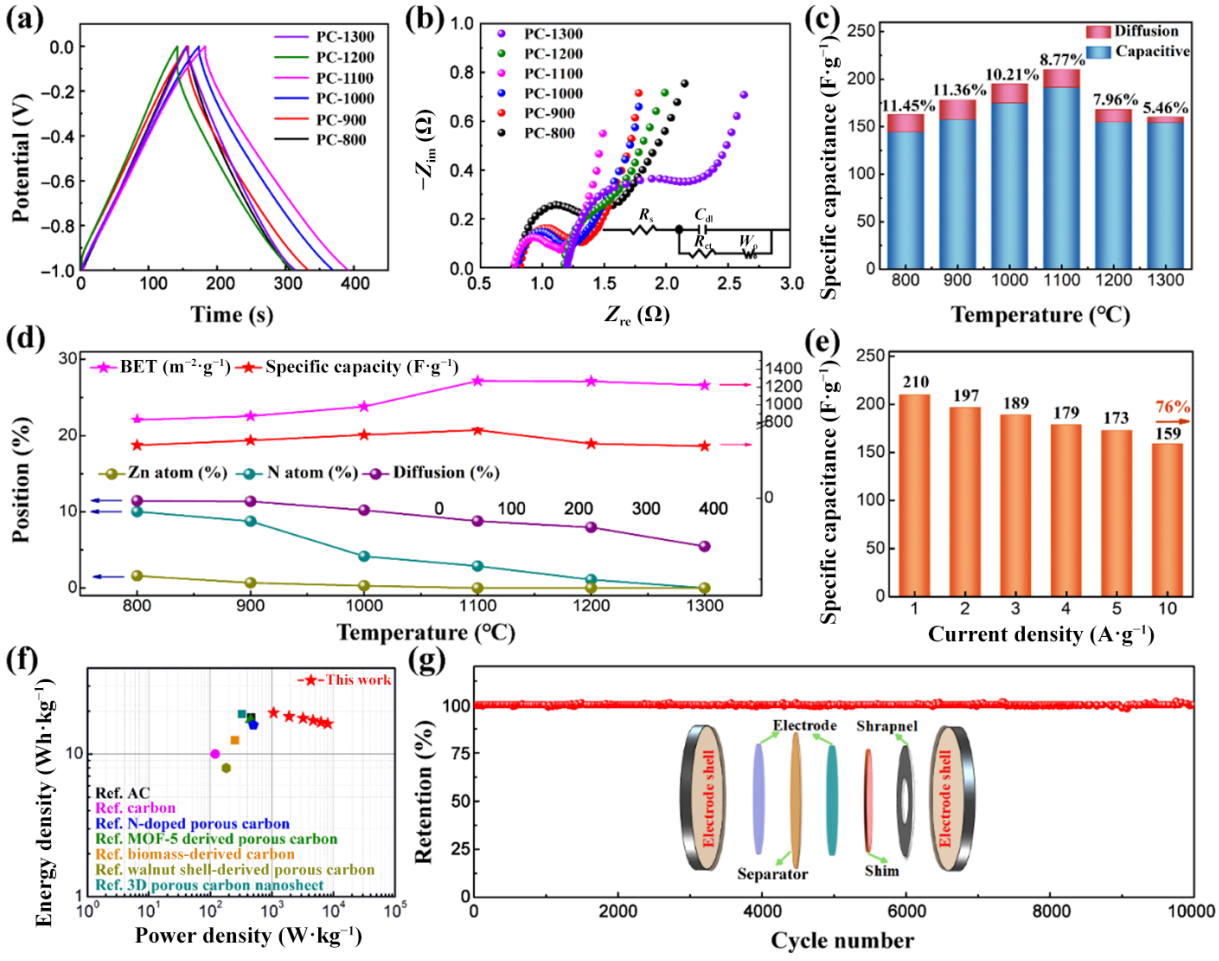

Figure 5 Electrochemical performance of ZIF-8-derived PC materials: (a) GCD curves at 1 A·g^{-1}. (b) Nyquist impedance plots. (c) Histograms of the capacitive and diffusion contributions for all the samples at a scan rate of 5 mV·s^{-1}. (d) Comparison of the specific surface area, specific capacitances, Zn and N element content, and diffusion contributions with temperature changes. (e) Specific capacitances of PC-1100 at different current densities. N-doped PC-1100//PC-1100 symmetric supercapacitor device: (f) Ragone plots of PC-1100//PC-1100 SSC and comparison with other carbon-based SSCs. (g) The cycling performance at 4.0 A·g^{-1} for 10,000 cycles (inset: schematic illustration).

electrolyte ions, enhance the charge transfer rate, and shorten the ion diffusion distance, resulting in improved charge transfer and diffusion processes with small R_{ct} and W_0 values. These fascinating features act synergistically to render the PC-1100 sample superior in electrochemical performance to all other samples. Figure S10(c) in the ESM shows the GCD curves of PC-1100 at different current densities. All the curves show a nearly symmetrical triangular shape, suggesting the EDLC characteristic with good reversibility and excellent Coulombic efficiency. Figure S10(d) in the ESM displays the CV curves of PC-1100 at different scan rates, which have no obvious redox peaks. Figure S10(e) in the ESM shows the cycling performance of PC-1100. After 10,000 cycles, the capacitance retention maintains nearly 100%, demonstrating the remarkable cycle stability.

According to the Dunn theory [40], the electrochemical kinetic process of electrode material in supercapacitors mainly involves capacitive contribution and diffusion-controlled contribution. The capacitive contribution is a fast-kinetic process, including ion adsorption/desorption (EDLC behavior) and highly reversible fast Faradaic reactions at the surface of electrodes. The diffusion-controlled contribution is a slow-kinetic process; this is intercalation pseudocapacitance with redox reaction in the electrode [41, 42]. The electrochemical kinetic process can be analyzed by fitting the CV curves. The relationship between current density ($i(V)$) and scan rate (v) can be described by Eq. (2) [43]

$$i(V) = kv + k'v^{0.5} \quad (2)$$

where k and k' are constants. The items of kv and $k'v^{0.5}$ are the contributions of fast-kinetic and slow-kinetic processes, respectively. Figure S11 in the ESM displays the CV curves of ZIF-8-derived PC materials at different temperatures, which are fitted by fast-kinetic and slow-kinetic processes. Figure 5(c) shows the typical histograms of the capacitive and diffusion contributions for all the samples at a scan rate of 5 mV·s^{-1}. The specific capacitance is mainly determined by capacitive contribution, further indicating the EDLC feature of ZIF-8-derived PC materials. Based on the elemental component, BET results, and microstructure, the relationship between specific surface area and specific capacities contribution shows that the specific capacities are positively related to the specific surface area. The content of Zn and N element is likewise positively related to the diffusion contribution (Fig. 5(d)). These results show that the diffusion contribution is positively relevant to the content of Zn–N_1 configuration. These results suggest that the high pyrolysis temperature can promote the volatilization of Zn element, creating more channels and porosity, thus enhancing the specific

surface area for ions adsorption/desorption and shortening the distance for ions migration. However, too high temperature may also cause the collapse of carbon skeleton, reducing the specific surface area. Proper pyrolysis temperature can improve the porosity and specific surface area of ZIF-8-derived PC materials, resulting in high specific capacitance. We consider that the capacitive contribution originates from the specific surface area, while the diffusion contribution is mainly attributed to the $Zn–N_1$ configuration. For PC-1300, no Zn or N elements are detected, but the diffusion contribution can also be found. This is probably mainly due to the fact that the volatilization of Zn and N elements may induce defects in the carbon skeleton, resulting in diffusion contribution. The above results show that the specific surface area and $Zn–N_1$ configuration synergistically boost the capacitive performance. The specific capacitances of PC-1100 at different current densities are summarized in Fig. 5(e). PC-1100 shows a good rate capability of 76% at 10 $A·g^{-1}$.

To further evaluate the potential applications, a coin-cell-type SSC was constructed. N-doped PC-1100 is used as both the positive and negative electrodes, and 6.0 M KOH is the electrolyte. The CV and GCD curves were performed in the potential range of 0–1.6 V. Figure S12(a) in the ESM shows the CV curves of N-doped PC-1100//PC-1100 SSC device measured at different scan rates. All the curves show quasi-rectangle with symmetric shape, indicating the typical capacitive characteristic with good reversibility at wide scan rates. The GCD curves at different current densities display nearly symmetric triangular shape, further suggesting the capacitive feature and high reversibility during the charging/discharging process (Fig. S12(b) in the ESM). Figure 5(f) shows the Ragone plots of N-doped PC-1100//PC-1100 SSC device. The energy density (E) can reach 19.4 $Wh·kg^{-1}$ at a power density (P_{dens}) of 1063 $W·kg^{-1}$, and it remains 16.3 $Wh·kg^{-1}$ at 8081 $W·kg^{-1}$. This is comparative or superior to other reported carbon-based SSCs [44–50]. The cycling performance of N-doped PC-1100//PC-1100 SSC (Fig. 5(g)) shows high capacitance retention of nearly 100% after 10,000 cycles at 4.0 $A·g^{-1}$, displaying an outstanding long-term cycling stability. Table S6 in the ESM gives a quantitative performance comparison with ZIF-derived carbon-based supercapacitors. Comparative analysis confirms that our porous carbon exhibits upper-medium capacitance, energy density/power density, and the most superior cycling stability [51–65].

Furthermore, DFT calculations were used to explore the electronic states and adsorption energies in alkaline environment of ZnNC. Based on the above coordination structure analyses, graphene layers with $Zn–N_1$ and $Zn–N_4$ structure models were built and optimized. The differential partial charge density analyses demonstrate that C/N atoms attract more electrons from the Zn center in the ZnNC (Figs. 6(a) and 6(b)). The charge distribution of $Zn–N_4$ structural model is more symmetrical compared with $Zn–N_1$ structural model (Figs. 6(c) and 6(d)). The Bader charge analyses display that the Zn center in the $Zn–N_4$ structural model carries more positive charges than that of $Zn–N_1$ and show the amount of charge of 1.16 and 0.95, respectively. These demonstrated that $Zn–N_1$ and $Zn–N_4$ structures have different charge environments. To prove the electrochemical reaction kinetics of ZnNC, Figs. 6(e) and 6(f) show the adsorption energy for OH^- of $Zn–N_1$ and $Zn–N_4$ structural model. Compared with structurally symmetrical $Zn–N_4$ (0.27 eV), $Zn–N_1$ has lower adsorption energy of −0.79 eV, indicating that $Zn–N_1$ structural model more likely to undergo redox reactions than $Zn–N_4$. Besides, the densities of states of C, N, and Zn atoms of ZnNC were calculated to exhibit electronic structures (Figs. 6(g) and 6(h)). Compared to the $Zn–N_4$, $Zn–N_1$ structural model possesses more abundant electrons at the Fermi level, indicating better electrical

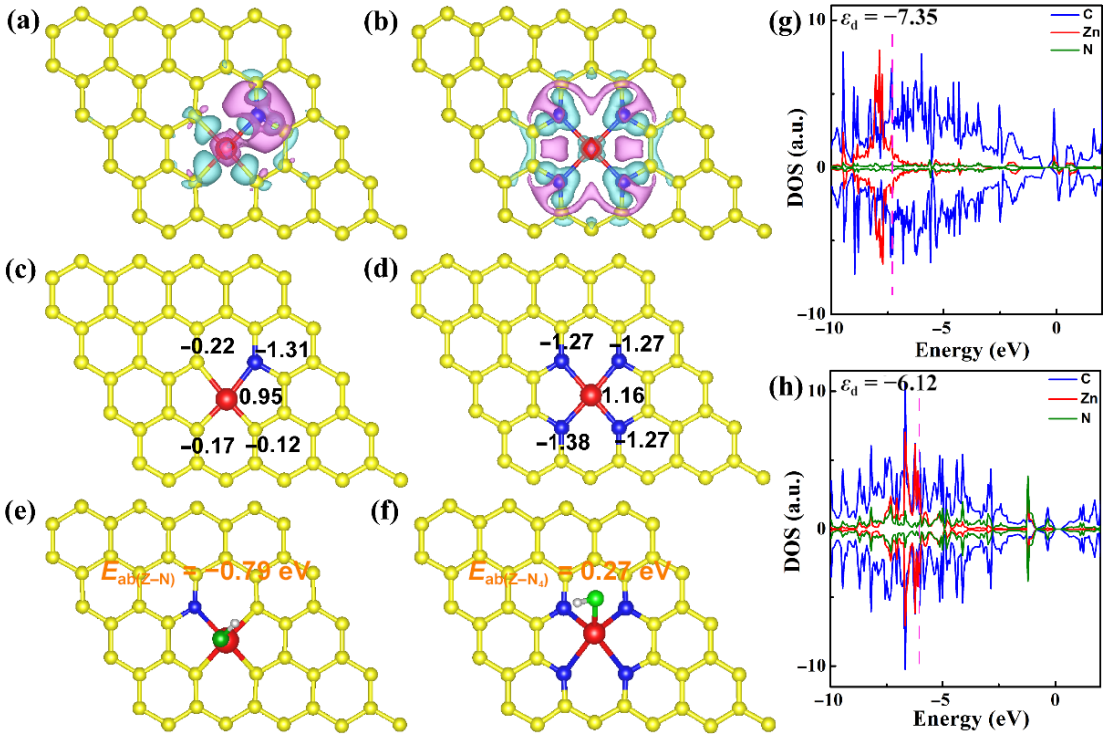

Figure 6 DFT calculations for ZnNC: differential partial charge density of (a) $Zn–N_1$ and (b) $Zn–N_4$ (cyan and purple areas represent the regions with charge density increase and reduction). Optimized structures and Bader charge of (c) $Zn–N_1$ and (d) $Zn–N_4$. Adsorption energy for OH^- of (e) $Zn–N_1$ and (f) $Zn–N_4$. Density of states of C, Zn, and N atoms of (g) $Zn–N_1$ and (h) $Zn–N_4$.

conductivity. Moreover, the d band center of Zn 3d orbitals of $Zn–N_1$ and $Zn–N_4$ structural model are −7.35 and −6.12 eV, respectively, which can be obtained by calculation. It indicates the different electron cloud distributions of $Zn–N_1$ and $Zn–N_4$. The above theoretical calculation results show that the $Zn–N_1$ configuration has higher redox activity than the original $Zn–N_4$ cluster.

4 Conclusions

In summary, ZIF-8-derived porous carbon was prepared by pyrolysis route for supercapacitors. The pyrolysis mechanisms of ZIF-8 were dynamically studied by *in situ* heating TEM and *ex situ* characterizations. During the pyrolysis process, the porous carbon maintains the pristine dodecahedral shape of ZIF-8 with large specific surface area and high porosity, during which Zn and N elements were decomposed out of the skeleton. However, residual Zn is still detectable at 1100 °C, which is far above the boiling point of Zn (907 °C). This result revises the traditional view of Zn volatilization in Zn-MOF-derived carbon, which claimed complete Zn removal above 907 °C. Cs-corrected HAADF-STEM image and synchrotron radiation indicate that the residual Zn element is uniformly anchored in the carbon skeleton as single Zn atom with $Zn–N_1$ configuration. Electrochemical performance indicates that the specific capacitance of ZIF-8-derived N-doped porous carbon is proportional to the specific surface area. The porous carbon synthesized at 1100 °C, which shows the highest specific surface area of 1269 $m^2·g^{-1}$, exhibits the highest specific capacitance of 210 $F·g^{-1}$ at 1.0 $A·g^{-1}$. A symmetric supercapacitor assembled by the optimal ZIF-8-derived porous carbon delivers an energy density of 19.4 $Wh·kg^{-1}$ at a power density of 1063 $W·kg^{-1}$, which also possesses excellent cycling stability of about 100% after 10,000 cycles. These results not only give a deep insight to the pyrolysis process of ZIF-8, but also are important to investigate the microstructural resolution of Zn-MOFs, which are significant to understand the properties and explore the applications of Zn-MOFs derived porous carbon.

Electronic Supplementary Material: Supplementary material (Figs. S1–S12: characterization of ZIF-8; Raman spectra, SEM images, EDX images, XPS spectra, N_2 sorption/adsorption isotherms, *ex situ* TEM images, XANES spectra, and electrochemical performance of ZIF-8-derived PC materials; and electrochemical performance of porous carbon and N-doped PC-1100//PC-1100 symmetric supercapacitor device; Tables S1–S6) is available in the online version of this article at https://doi.org/10.26599/NR.2026.94908497.

Data availability

All data needed to support the conclusions in the paper are presented in the manuscript and the Electronic Supplementary Material. Additional data related to this paper may be requested from the corresponding author upon request.

Acknowledgements

This work was supported by the Natural Science Foundation of Shaanxi Province (Nos. 2025JC-YBQN-057 and 2025JC-YBMS-106).

Declaration of competing interest

All the contributing authors report no conflict of interests in this work.

Author contribution statement

H. N. X.: Formal analysis, data curation, writing – original draft, investigation. Y. B. L.: Formal analysis, data curation, investigation. X. D.: Validation, Methodology. X. C.: Software, supervision. Y. Z.: Data curation, software. J. F.: Formal analysis, methodology. X. H. Z.: Project administration, validation. X. H. L.: Conceptualization, writing – review & editing, supervision. H. Y. Z.: Methodology, validation. X. L. Z.: Project administration, supervision. All the authors have approved the final manuscript.

Use of AI statement

None.

References

[1] Ren, J. C.; Huang, Y. L.; Zhu, H.; Zhang, B. H.; Zhu, H. K.; Shen, S. H.; Tan, G. Q.; Wu, F.; He, H.; Lan, S. et al. Recent progress on MOF-derived carbon materials for energy storage. *Carbon Energy* **2020**, *2*, 176–202.

[2] Song, X. K.; Jiang, Y.; Cheng, F.; Earnshaw, J.; Na, J.; Li, X. P.; Yamauchi, Y. Hollow carbon-based nanoarchitectures based on ZIF: Inward/outward contraction mechanism and beyond. *Small* **2021**, *17*, 2004142.

[3] Li, C. B.; Ji, Y.; Wang, Y. P.; Liu, C. X.; Chen, Z. Y.; Tang, J. L.; Hong, Y. W.; Li, X.; Zheng, T. T.; Jiang, Q. et al. Applications of metal–organic frameworks and their derivatives in electrochemical CO_2 reduction. *Nano-Micro Lett.* **2023**, *15*, 113.

[4] Wang, X. H.; Huang, F. F.; Rong, F.; He, P.; Que, R. H.; Jiang, S. P. Unique MOF-derived hierarchical MnO_2 nanotubes@NiCo-LDH/CoS_2 nanocage materials as high performance supercapacitors. *J. Mater. Chem. A* **2019**, *7*, 12018–12028.

[5] Cao, X. H.; Tan, C. L.; Sindoro. M.; Zhang, H. Hybrid micro-nano-structures derived from metal–organic frameworks: Preparation and applications in energy storage and conversion. *Chem. Soc. Rev.* **2017**, *46*, 2660–2677.

[6] Yan, Y.; Gu, P.; Zheng, S. S.; Zheng, M. B.; Pang, H.; Xue, H. G. Facile synthesis of an accordion-like Ni-MOF superstructure for high-performance flexible supercapacitors. *J. Mater. Chem. A* **2016**, *4*, 19078–19085.

[7] Jin, Z. K.; Dong, W. J.; Yang, M.; Wang, J. J.; Gao, H. Y.; Wang, G. One-pot preparation of hierarchical nanosheet-constructed Fe_3O_4/MIL-88B(Fe) magnetic microspheres with high efficiency photocatalytic degradation of dye. *ChemCatChem* **2016**, *8*, 3510–3517.

[8] Wu, M. X.; Li, J.; Liu, Z. Y.; Liu, H. Z.; Wang, G. D.; Ma, J. F. Boron doped partially wrapped hierarchical porous carbon materials towards oxygen reduction reaction. *J. Electroanal. Chem.* **2023**, *938*, 117456.

[9] Chu, K. N.; Hu, M. L.; Song, B.; Chen, S. L.; Li, J. Y.; Zheng, F. C.; Li, Z. Q.; Li, R.; Zhou, J. Y. MOF-derived nitrogen-doped porous carbon nanofibers with interconnected channels for high-stability Li^+/Na^+ battery anodes. *RSC Adv.* **2023**, *13*, 5634–5642.

[10] Liu, Y. Y.; Gonçalves, A. A. S.; Zhou, Y.; Jaroniec, M. Importance of surface modification of γ-alumina in creating its nanostructured composites with zeolitic imidazolate framework ZIF-67. *J. Colloid Interface Sci.* **2018**, *526*, 497–504.

[11] Sun, D. R.; Sun, F. X.; Deng, X. Y.; Li, Z. H. Mixed-metal strategy on metal–organic frameworks (MOFs) for functionalities expansion: Co substitution induces aerobic oxidation of cyclohexene over inactive Ni-MOF-74. *Inorg. Chem.* **2015**, *54*, 8639–8643.

[12] Hou, S. L.; Wu, Y. N.; Feng, L. Y.; Chen, W.; Wang, Y.; Morlay, C.; Li, F. T. Green synthesis and evaluation of an iron-based metal–organic framework MIL-88B for efficient decontamination of arsenate from water. *Dalton Trans.* **2018**, *47*, 2222–2231.

[13] Yang, Q. H.; Yang, C. C.; Lin, C. H.; Jiang, H. L. Metal–organic-framework-derived hollow N-doped porous carbon with ultrahigh concentrations of single Zn atoms for efficient carbon dioxide conversion. *Angew. Chem., Int. Ed.* **2019**, *58*, 3511–3515.

[14] Xia, M.; Muhammad, F.; Zeng, L. H.; Li, S.; Huang, X.; Jiao, B. Q.; Shiau, Y.; Li, D. W. Solidification/stabilization of lead-zinc smelting slag in composite based geopolymer. *J. Cleaner Prod.* **2019**, *209*, 1206–1215.

[15] Wang, Q.; Ina, T.; Chen, W. T.; Shang, L.; Sun, F. F.; Wei, S. H.; Sun-Waterhouse, D.; Telfer, S. G.; Zhang, T. R.; Waterhouse, G. I. N. Evolution of Zn(II) single atom catalyst sites during the pyrolysis-induced transformation of ZIF-8 to N-doped carbons. *Sci. Bull.* **2020**, *65*, 1743–1751.

[16] Gadipelli, S.; Guo, Z. X. Tuning of ZIF-derived carbon with high activity, nitrogen functionality, and yield—A case for superior CO_2 capture. *ChemSusChem* **2015**, *8*, 2123–2132.

[17] Wang, X. Y.; Yuan, F. S.; Xue, D.; Liu, J.; Wei, J.; Wang, Y. W.; Wang, J. H.; Qu, Q. H.; Zhang, Q. L. MnO_2 nanoflowers decorated on ZIF-8-ZnO with Ni foam support for high-performance supercapacitors. *ChemNanoMat* **2022**, *8*, e202200243.

[18] Liang, Y.; Wei, J.; Hu, Y. X.; Chen, X. F.; Zhang, J.; Zhang, X. Y.; Jiang, J. P.; Tao, S. W.; Wang, H. T. Metal-polydopamine frameworks and their transformation to hollow metal/N-doped carbon particles. *Nanoscale* **2017**, *9*, 5323–5328.

[19] Kaneti, Y. V.; Tang, J.; Salunkhe, R. R.; Jiang, X. C.; Yu, A. B.; Wu, K. C. W.; Yamauchi, Y. Nanoarchitectured design of porous materials and nanocomposites from metal–organic frameworks. *Adv. Mater.* **2017**, *29*, 1604898.

[20] Wang, Y. F.; Liang, Y. Y.; Wu, Y. F.; Yang, J.; Zhang, X.; Cai, D. D.; Peng, X.; Kurmoo, M.; Zeng, M. H. *In situ* pyrolysis tracking and real-time phase evolution: From a binary zinc cluster to supercapacitive porous carbon. *Angew. Chem., Int. Ed.* **2020**, *59*, 13232–13237.

[21] Park, K. S.; Ni, Z.; Côté, A. P.; Choi, J. Y.; Huang, R. D.; Uribe-Romo, F. J.; Chae, H. K.; O'Keeffe, M.; Yaghi, O M. Exceptional chemical and thermal stability of zeolitic imidazolate frameworks. *Proc. Natl. Acad. Sci. USA* **2006**, *103*, 10186–10191.

[22] Zhu, W. K.; Kim, D.; Han, M. S.; Jang, J.; Choi, H.; Kwon, G.; Jeon, Y.; Yeol Ryu, D.; Lim, S. H.; You, J. et al. Fibrous cellulose nanoarchitectonics on N-doped carbon-based metal-free catalytic nanofilter for highly efficient advanced oxidation process. *Chem. Eng. J.* **2023**, *460*, 141593.

[23] Chaikittisilp, W.; Hu, M.; Wang, H. J.; Huang, H. S.; Fujita, T.; Wu, K. C. W.; Chen, L. C.; Yamauchi, Y.; Ariga, K. Nanoporous carbons through direct carbonization of a zeolitic imidazolate framework for supercapacitor electrodes. *Chem. Commun.* **2012**, *48*, 7259–7261.

[24] Zhao, Q.; Huang, S. Y.; Han, X. X.; Chen, J. J.; Wang, J. H.; Rykov, A.; Wang, Y.; Wang, M. Y.; Lv, J.; Ma, X. B. Highly active and controllable MOF-derived carbon nanosheets supported iron catalysts for Fischer-Tropsch synthesis. *Carbon* **2021**, *173*, 364–375.

[25] Zhang, Z. J.; Li, P. W.; Zhao, T.; Xia, Y. H. Enhanced CO_2 adsorption and selectivity of CO_2/N_2 on amine@ZIF-8 materials. *Adsorpt. Sci. Technol.* **2022**, *2022*, 3207986.

[26] Ronte, A.; Dangwal, S.; Lin, H.; Wagle, P.; Echeverria, E.; Lee, J. S.; Zhu, J. H.; Mcilroy, D. N.; Kim, S. J. Modification of ZIF-8 membranes by atomic layer deposition for high propylene/propane selectivity. *Micropor. Mesopor. Mater.* **2022**, *343*, 112173.

[27] Zhang, D. L.; Zhu, Y. H.; Liu, L. M.; Ying, X. R.; Hsiung, C. E.; Sougrat, R.; Li, K.; Han, Y. Atomic-resolution transmission electron microscopy of electron beam-sensitive crystalline materials. *Science* **2018**, *359*, 675–679.

[28] Zhu, Y. H.; Ciston, J.; Zheng, B.; Miao, X. H.; Czarnik, C.; Pan, Y. C.; Sougrat, R.; Lai, Z. P.; Hsiung, C. E.; Yao, K. X. et al. Unravelling surface and interfacial structures of a metal–organic framework by transmission electron microscopy. *Nat. Mater.* **2017**, *16*, 532–536.

[29] Liang, C. H.; Tang, Y.; Zhang, X. D.; Chai, H. X.; Huang, Y. M.; Feng, P. ZIF-mediated N-doped hollow porous carbon as a high performance adsorbent for tetracycline removal from water with wide pH range. *Environ. Res.* **2020**, *182*, 109059.

[30] Wang, D.; Zhao, Z. Y.; Wang, P.; Wang, S. M.; Feng, M. Synthesis of MOF-derived nitrogen-doped carbon microtubules via template self-consumption. *Rare Met.* **2022**, *41*, 2582–2587.

[31] Li, J.; Chen, S. G.; Yang, N.; Deng, M. M.; Ibraheem, S.; Deng, J. H.; Li, J.; Li, L.; Wei, Z. D. Ultrahigh-loading zinc single-atom catalyst for highly efficient oxygen reduction in both acidic and alkaline media. *Angew. Chem., Int. Ed.* **2019**, *58*, 7035–7039.

[32] Li, Z. G.; Wang, D. N.; Li, H. F.; Ma, M.; Zhang, Y.; Yan, Z. F.; Agnoli, S.; Zhang, G. X.; Sun, X. M. Single-atom Zn for boosting supercapacitor performance. *Nano Res.* **2022**, *15*, 1715–1724.

[33] Lee, J. S. M.; Briggs, M. E.; Hu, C. C.; Cooper, A. I. Controlling electric double-layer capacitance and pseudocapacitance in heteroatom-doped carbons derived from hypercrosslinked microporous polymers. *Nano Energy* **2018**, *46*, 277–289.

[34] Liu, Y. X.; Xiao, Z. C.; Liu, Y. C.; Fan, L. Z. Biowaste-derived 3D honeycomb-like porous carbon with binary-heteroatom doping for high performance flexible solid-state supercapacitors. *J. Mater. Chem. A* **2018**, *6*, 160–166.

[35] Feng, L. X.; Wang, K.; Zhang, X.; Sun, X. Z.; Li, C.; Ge, X. B.; Ma, Y. W. Flexible solid-state supercapacitors with enhanced performance from hierarchically graphene nanocomposite electrodes and ionic liquid incorporated gel polymer electrolyte. *Adv. Funct. Mater.* **2018**, *28*, 1704463.

[36] Wen, Y. L.; Chen, X. C.; Mijowska, E. Insight into the effect of ZIF-8 particle size on the performance in nanocarbon-based supercapacitors. *Chem.—Eur. J.* **2020**, *26*, 16328–16337.

[37] Wang, M.; Xue, R.; Guo, H.; Yang, W. A long-life pseudocapacitive triazine-based porous organic framework and resulting N-doped microporous carbons for supercapacitance application. *Funct. Mater. Lett.* **2019**, *12*, 1950065.

[38] Zhao, X. J.; Wan, H. Z.; Liang, P.; Wang, N. Z.; Wang, C.; Gan, Y.; Chen, X.; Tan, Q. Y.; Liu, X.; Zhang, J. et al. Favorable anion adsorption/desorption of high rate $NiSe_2$ nanosheets/hollow mesoporous carbon for battery-supercapacitor hybrid devices. *Nano Res.* **2021**, *14*, 2574–2583.

[39] Ouyang, Y.; Huang, R. J.; Xia, X. F.; Ye, H. T.; Jiao, X. Y.; Wang, L.; Lei, W.; Hao, Q. L. Hierarchical structure electrodes of NiO ultrathin nanosheets anchored to $NiCo_2O_4$ on carbon cloth with excellent cycle stability for asymmetric supercapacitors. *Chem. Eng. J.* **2019**, *355*, 416–427.

[40] Augustyn, V.; Simon, P.; Dunn, B. Pseudocapacitive oxide materials for high-rate electrochemical energy storage. *Energy Environ. Sci.* **2014**, *7*, 1597–1614.

[41] Kim, H. S.; Cook, J. B.; Lin, H.; Ko, J.; Tolbert, S.; Ozolins, V.; Dunn, B. Oxygen vacancies enhance pseudocapacitive charge storage properties of MoO_{3-x}. *Nat. Mater.* **2017**, *16*, 454–460.

[42] Zhang, H. Q.; Liu, X. H.; Chen, Y. D.; Kuang, H. F.; Zhen, H. Y.; Zhang, W. G.; Chen, H.; Ling, Q. D. Construction of core–shell heterostructure containing sandwich-like nanoarray for high-performance supercapacitors. *J. Energy Storage* **2023**, *67*, 107647.

[43] Lin, T. Q.; Chen, I. W.; Liu, F. X.; Yang, C. Y.; Bi, H.; Xu, F. F.; Huang, F. Q. Nitrogen-doped mesoporous carbon of extraordinary capacitance for electrochemical energy storage. *Science* **2015**, *350*, 1508–1513.

[44] Daraghmeh, A.; Hussain, S.; Saadeddin, I.; Servera, L.; Xuriguera, E.; Cornet, A.; Cirera, A. A study of carbon nanofibers and active carbon as symmetric supercapacitor in aqueous electrolyte: A comparative study. *Nanoscale Res. Lett.* **2017**, *12*, 639.

[45] Wang, D. W.; Min, Y. G.; Yu, Y. H. Facile synthesis of wheat bran-derived honeycomb-like hierarchical carbon for advanced symmetric supercapacitor applications. *J. Solid State Electrochem.* **2015**, *19*, 577–584.
[46] Yu, F.; Wang, T.; Wen, Z. B.; Wang, H. X. High performance all-solid-state symmetric supercapacitor based on porous carbon made from a metal–organic framework compound. *J. Power Sources* **2017**, *364*, 9–15.
[47] Shang, Z.; An, X. Y.; Zhang, H.; Shen, M. X.; Baker, F.; Liu, Y. X.; Liu, L. Q.; Yang, J.; Cao, H. B.; Xu, Q. L. et al. Houttuynia-derived nitrogen-doped hierarchically porous carbon for high-performance supercapacitor. *Carbon* **2020**, *161*, 62–70.
[48] Hao, J. Y.; Wang, B. X.; Xu, H.; Du, J. C.; Wu, C.; Qin, W.; Wu, X. Q. Interfacial regulation of biomass-derived carbon towards high-performance supercapacitor. *J. Energy Storage* **2024**, *86*, 111301.
[49] Fu, H. H.; Chen, L.; Gao, H. J.; Yu, X. K.; Hou, J.; Wang, G.; Yu, F.; Li, H. Q.; Fan, C. C.; Shi, Y. L. et al. Walnut shell-derived hierarchical porous carbon with high performances for electrocatalytic hydrogen evolution and symmetry supercapacitors. *Int. J. Hydrogen Energy* **2020**, *45*, 443–451.
[50] Zhang, P.; Wang, W. X.; Kou, Z. M.; Wang, B.; Zhong, X. B. Low-cost and advanced symmetry supercapacitors based on three-dimensional tea waste of porous carbon nanosheets. *Mater. Technol.* **2021**, *36*, 1–10.
[51] Salunkhe, R. R.; Kamachi, Y.; Torad, N. L.; Hwang, S. M.; Sun, Z. Q.; Dou, S. X.; Kim, J. H.; Yamauchi, Y. Fabrication of symmetric supercapacitors based on MOF-derived nanoporous carbons. *J. Mater. Chem. A* **2014**, *2*, 19848–19854.
[52] Zhu, F. F.; Liu, W. J.; Liu, Y.; Shi, W. D. Construction of porous interface on CNTs@NiCo-LDH core–shell nanotube arrays for supercapacitor applications. *Chem. Eng. J.* **2020**, *383*, 123150.
[53] Li, Y. Q.; Wei, Z. H.; Chen, X. Q.; Li, S. H.; Pang, S. P. Porous hybrid carbon nanofibers derived from metal–organic frameworks for high-performance supercapacitors. *J. Alloys Compd.* **2022**, *925*, 166766.
[54] Xue, C. F.; Zhao, W.; Zhang, Q.; Wang, J. X.; Wei, Y. Y.; Lv, K.; Wu, T.; Lin, Y.; Li, X. H.; Hao, X. G. From salt-filled ZIF-8 to open-door nanoporous carbon with optimized pore system for electrochemical supercapacitor with enhanced energy density. *J. Energy Storage* **2022**, *51*, 104421.
[55] Shang, M. G.; Zhang, X. N.; Zhang, J.; Sun, J. Q.; Zhao, X. F.; Yu, S. M.; Liu, X. C.; Liu, B. X.; Yi, X. B. Nitrogen-doped carbon composite derived from ZIF-8/polyaniline@cellulose-derived carbon aerogel for high-performance symmetric supercapacitors. *Carbohydr. Polym.* **2021**, *262*, 117966.
[56] Choi, H. S.; Kim, Y. H.; Kim, H. K.; Kim, K. B. Assembly of graphene-wrapped ZIF-8 microspheres and confined carbonization for energy storage applications. *J. Power Sources* **2023**, *560*, 232702.
[57] Zhang, D. L.; Zhang, J. H.; Pan, M. D.; Wang, Y.; Sun, T. Necklace-like C-ZIF-8@MWCNTs fabricated by electrochemical deposition towards enhanced supercapacitor. *J. Alloys Compd.* **2021**, *853*, 157368.
[58] Yue, Y.; Huang, Y. L.; Bian, S. W. Nitrogen-doped hierarchical porous carbon films derived from metal–organic framework/cotton composite fabrics as freestanding electrodes for flexible supercapacitors. *ACS Appl. Electron. Mater.* **2021**, *3*, 2178–2186.
[59] Wang, Y.; Qiao, M. F.; Mamat, X. Nitrogen-doped macro-meso-micro hierarchical ordered porous carbon derived from ZIF-8 for boosting supercapacitor performance. *Appl. Surf. Sci.* **2021**, *540*, 148352.
[60] Otun, K. O.; Xaba, M. S.; Zong, S.; Liu, X. Y.; Hildebrandt, D.; El-Bahy, S. M.; Alotaibi, M. T.; El-Bahy, Z. M. ZIF-8-derived ZnO/C decorated hydroxyl-functionalized multi-walled carbon nanotubes as a new composite electrode for supercapacitor application. *Colloid Interface Sci. Commu.* **2022**, *47*, 100589.
[61] Hsiao, Y. J.; Lin, L. Y. Efficient pore engineering in carbonized zeolitic imidazolate framework-8 via chemical and physical methods as active materials for supercapacitors. *J. Power Sources* **2021**, *486*, 229370.
[62] Shang, Z.; An, X. Y.; Liu, L. Q.; Yang, J.; Zhang, W.; Dai, H. Q.; Cao, H. B.; Xu, Q. L.; Liu, H. B.; Ni, Y. H. Chitin nanofibers as versatile bio-templates of zeolitic imidazolate frameworks for N-doped hierarchically porous carbon electrodes for supercapacitor. *Carbohydr. Polym.* **2021**, *251*, 117107.
[63] Wang, L.; Wang, C. X.; Wang, H. F.; Jiao, X. Y.; Ouyang, Y.; Xia, X. F.; Lei, W.; Hao, Q. L. ZIF-8 nanocrystals derived N-doped carbon decorated graphene sheets for symmetric supercapacitors. *Electrochim. Acta* **2018**, *289*, 494–502.
[64] Wu, J.; Zhang, X. P.; Wei, F. X.; Sui, Y.; Qi, J. Q. Controllable synthesis of ZIF-derived nano-hexahedron porous carbon for supercapacitor electrodes. *Mater. Lett.* **2020**, *258*, 126761.
[65] Ahmad, R.; Iqbal, N.; Noor, T.; Ali, G.; Ali, M.; Shahzad, N.; Raza, M. A. Zeolitic imidazolate frameworks derived Co-Zn-nanoporous carbon-sulfide material for supercapacitors. *Electrochim. Acta* **2022**, *404*, 139739.